



OPEN

SUBJECT AREAS:
STRUCTURAL PROPERTIES
FLUIDICSReceived
26 August 2014Accepted
3 October 2014Published
24 October 2014Correspondence and
requests for materials
should be addressed to
G.Z. (gang@jlu.edu.
cn)

Real-Time Control of Uni-Directional Liquid Spreading on a Half-Cone Nanoshell Array

Bin Ai¹, Limin Wang¹, Helmuth Möhwald², Ye Yu¹, Zhiyuan Zhao³, Ziwei Zhou¹, Gang Zhang¹ & Quan Lin¹¹State Key Lab of Supramolecular Structure and Materials, College of Chemistry Jilin University, Changchun 130012, P.R. China, ²Max Planck Institute of Colloids and Interfaces D-14424 Potsdam, Germany, ³Stratingh Institute for Chemistry, and Zernike Institute for Advanced Materials, University of Groningen, Nijenborgh 4, 9747 AG Groningen, The Netherlands.

Half-cone nanoshell arrays, fabricated by a simple and efficient colloidal lithography method, enable uni-directional liquid spreading on their hydrophilic asymmetric nanostructured surface. The preferred direction of the liquid flow is reversed when the surface is made hydrophobic. Accordingly, poly(N-isopropyl-acrylamide) is polymerized onto the surface for in-site controlling the transition of liquid spreading direction via its temperature dependent hydrophobicity. Furthermore, we also explain theoretically, that the spreading direction on hexagonal nanocone arrays is independent of the lattice orientation and only depends on the slanting direction. The insights gained from this work offer new opportunities for smart microfluidics, water harvesting and making use of other wetting conditions on demand.

Anisotropically wetting surfaces have attracted a lot of attention owing to their advantages of directing flow in microfluidic devices, evaporation driven formation of patterns, and easy-to-clean coatings as well as to their fundamental interest^{1–6}. They can be achieved by various micro/nanoscale topographic features^{7–11} and selective chemical patterning on surfaces^{12,13}. In addition, groove geometries and patterned surface chemistries have produced anisotropic wetting, where contact-angle variations in different directions resulted in elongated droplet shapes^{14–21}. In all of these studies, however, the wetting behavior preserves left–right symmetry. Recently, very interesting wetting phenomena of uni-directional liquid spreading (the liquid propagates in a single preferred direction and pins in all others) were observed on slanting micro-pillar arrays²². In this approach, various inclined nanostructures in the form of slanting nanorods or nanopillars have been fabricated to develop the uni-directional spreading^{23–27}. These impressive efforts have been made for understanding the fundamental uni-directional behavior and wetting mechanism. However, real-time control as well as switching of the uni-directional liquid flow based on inclined nanostructures has not been realized. On the other hand deeper understanding and further examination of the wetting behavior of the inclined nanostructures are required for extensive potential applications. A special challenge will be to have simple and reproducible manufacturing tools and to be able to switch and to control liquid flow.

To address these issues, we present herein a well-designed half-cone nanoshell array to achieve multifunctional wetting. The novel inclined nanostructures are fabricated via a versatile, simple and efficient colloidal lithography (CL) technique^{28–30} (details shown in Supplementary Fig. S1 online). *In-site* and immediate control of the uni-directional liquid flow is realized by decorating the surface with poly(N-isopropyl-acrylamide) (PNIPAAm), which results in real-time temperature switchable wetting behavior, yet on the same nanostructures. This property is expected to be greatly advantageous to achieve complex flow patterns, wetting on demand and pave a new way for smart microfluidics. Furthermore, we also explain theoretically, that the spreading direction on the hexagonal half-cone nanoshell arrays is independent of the lattice orientation and only depends on the slanting direction. The insights gained from this work not only expand the inclined structures but also develop the theory.

Results

First, we focus on the water spreading on the novel structure when the surface is hydrophobic. Figure 1A shows the SEM image of the half-cone nanoshell array and the main structural parameters. When 3 μ L water is deposited on the sample under the condition that the shells slant to $-X$, the water droplet shows an obvious trend of spreading to $+X$ shown in Figure 1B. The left contact angle (CA) is 85° and the right CA is 97°. In the

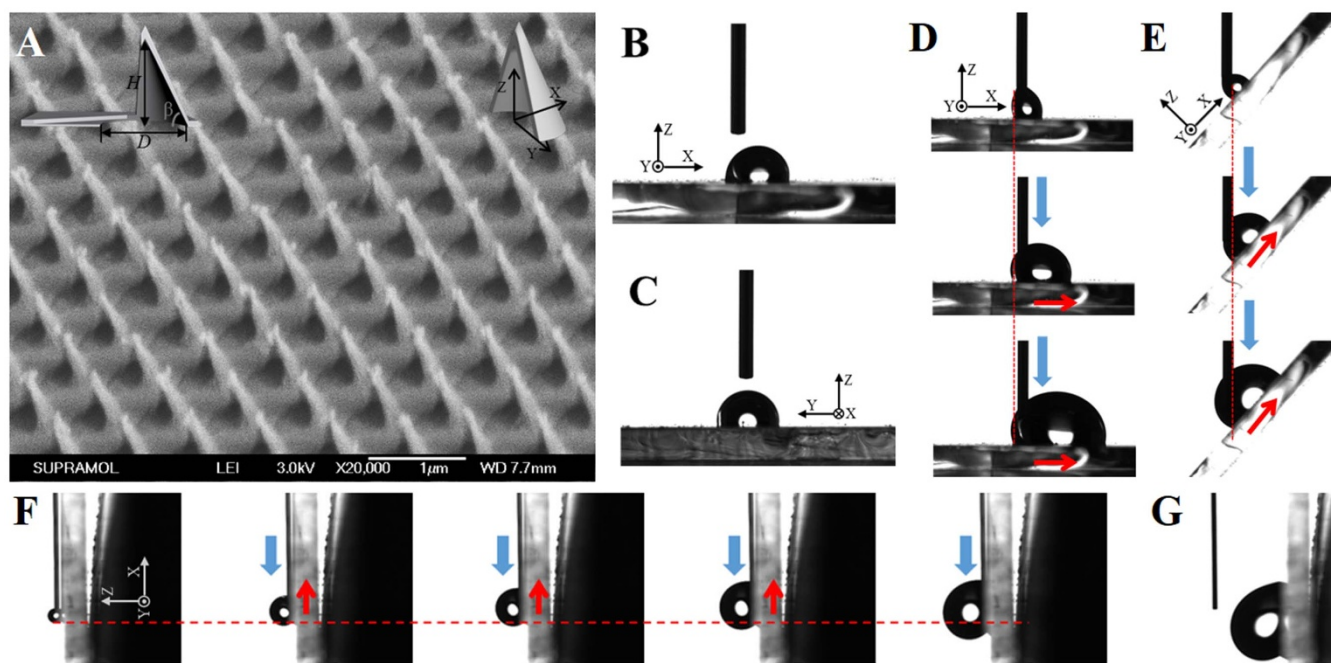


Figure 1 | Water spreading on a hydrophobic half-cone nanoshell array. (A) SEM image of the half-cone nanoshell array. The image is taken from a 45° tilting view. The left inset schematic shows the cross section of a single half-cone nanoshell and the main structural parameters. The right inset schematic shows the coordinate system. The height $H = 600$ nm; diameter $D = 400$ nm; $\beta \approx 72^\circ$. Side views of a sessile droplet on the surface taken from (B) X-Z plane and (C) Y-Z plane. The nanoshells slant to $-X$. *In-situ* photographs of the water droplet taken at different time after the water droplet contacted the substrate along the horizontal plane and (E) the substrate inclined with 50° and (F) 90° from the horizontal plane. The nanoshells slant to $-X$ in (D–F). The red dotted lines in (D–F) indicate the unchanged pinned position. The blue and red arrows indicate the injecting direction and water moving direction, respectively. The coordinate in (B–F) shows the orientation of nanoshells and corresponds to the right inset image in (A).

image taken from the Y-Z plane (Figure 1C), the left and right CA are both 98° , showing no asymmetric wetting behavior. These results indicate that the sample shows a preferred water spreading direction which is towards the reverse of the slanting direction. In particular as soon as the droplet touches the surface, it shows an obvious shift to $+X$ (Figure 1D). As water is injected ($1 \mu\text{L/s}$) continuously in Figure 1E and F, only the three-phase contact line at the $+X$ direction moves forward while another contact line at the $-X$ side pins on the surface, which means the advancing angle of water on the asymmetric surface is anisotropic (Supplementary Video 1 online) (the video is accelerated by four times, which also applies to videos 1, 2, 7 and 11–14). When the substrate is inclined with 50° from the horizontal plane, as shown in Figure 1E, the contact line of the water droplet also moves upward (Supplementary Video 2 online). To further illustrate the anisotropic wetting property of the surface, water is injected downward at a speed of $0.5 \mu\text{L/s}$ to the vertical substrate in Figure 1F, the droplet still moves upward despite the gravity and the downward injecting force (Supplementary Video 3 online). When water is injected to $6 \mu\text{L}$, as shown in the last image of Figure 1F, the droplet begins to move downward. Besides the droplet ($10 \mu\text{L}$) would hang on the substrate when stopping injection, showing strong adhesion on the half-cone nanoshell structure (Figure 1G).

The evolution of the CA and baselines is measured while injecting and sucking water at a speed of $0.5 \mu\text{L/s}$ for more clarity of the water moving process. Figure 2A shows the left and right CA and baselines while injecting water in the X-Z plane (Supplementary Video 4 online). As continuously injecting water, the left and right CA both increase till the baseline moves. The right baseline begins to move at the right CA = 104° and left CA = 93° while the distance to the left edge of the left baseline keeps the same. In the moving process, the liquid front gradually migrates to the reverse of the slanting direction at a speed of 0.12 mm/s with the other pins to the surface for the

whole process. Furthermore, the right CA experiences fluctuation while moving, which demonstrates the spreading is a stick-slip behavior. At the same time, the left CA is always smaller than the right CA and shows a slightly decreasing trend. In the sucking process in Figure 2B, the right CA is larger than the left CA at beginning. Then the right and left CA both show an obvious decreasing trend and become the same at last. The left baseline moves prior to the right baseline at the left CA = 11° . The right baseline moves at the right CA = 16° . So the right hysteresis CA = $104 - 16 = 88^\circ$. The large hysteresis CA demonstrates the strong adhesion of the hydrophobic sample and the state of the droplet on the Ag half-cone nanoshell array fits to Wenzel model³¹. For the injecting and sucking processes in the Y-Z planes in Figure 2C and D (Supplementary Video 5 and 6 online), the left and right CA and baselines show the same changing behavior. This demonstrates there is no asymmetric wetting property in the Y-Z plane. The advancing CA is 117° and the receding CA is 22° . So the hysteresis CA is 95° , which also demonstrates the strong adhesion and the state of the droplet on the Ag half-cone nanoshell array fits to Wenzel model. In particular, the advancing speed along the Y direction is 0.2 mm/s (for one side), which is one-sixth of the speed along the X direction. This demonstrates the well uni-directional spreading property.

When the surface is modified with trichloro(1H, 1H, 2H, 2H-perfluorooctyl) silane (PFS), the sample becomes superhydrophobic and possesses a weak adhesive force between the sample and the droplet (Supplementary Video 7 and 8 online). The CA becomes 153° ; the advancing CA is 158° ; the receding CA is 145° ; the hysteresis CA is 13° ; the sliding angle is 6° ; and the anisotropic wetting behavior disappears (Supplementary Fig. S2 online). These results demonstrate that water would not enter into the interspacing between the nanostructures and is only supported by the tips of the nanoshells, which fits to the Cassie model³². However, if water enters into the interspacing, which is Wenzel or semi-Wenzel model,

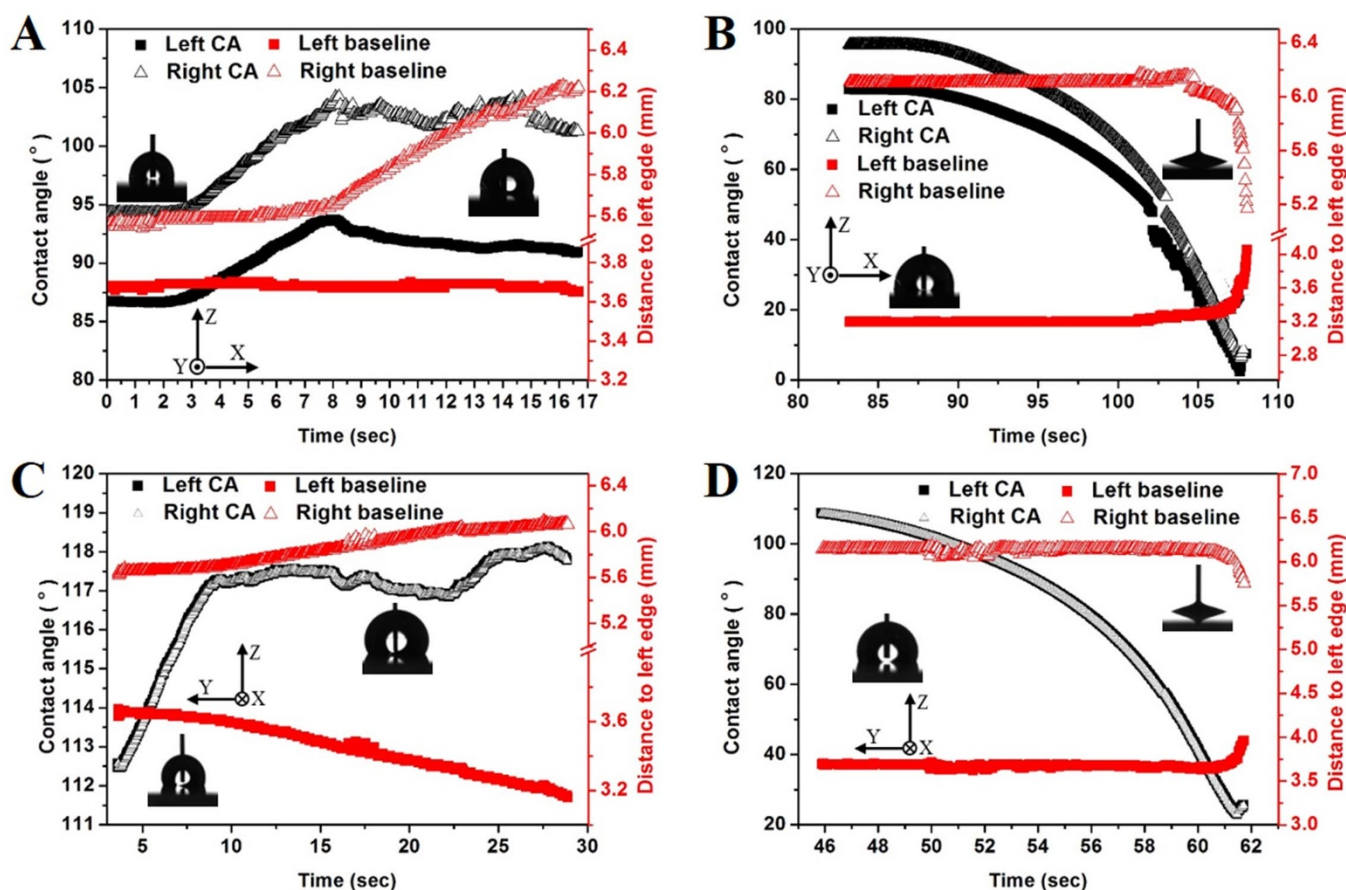


Figure 2 | The evolution of the CA and baselines: while (A) injecting and (B) sucking water for the X-Z plane and while (C) injecting and (D) sucking water for the Y-Z plane. The inset images show the initial state and moving state. The right axis indicates the distance of the pinned position to the left edge of the camera visual field. The coordinate shows the orientation of nanoshells and corresponds to the right inset image in Figure 1A. The nanoshells all slant to $-X$.

the nanoshell structure would play its role to lead to the asymmetric wetting property. Cassie model could remove the effect of the asymmetric structure, making the wetting behavior homogeneity. So the anisotropic wetting behavior disappears on the superhydrophobic half-cone nanoshell arrays because of the transition from the Wenzel model (the condition on the naked Ag surface in Figure 1) to the Cassie model. The water droplet would not slip along the shell but only can be supported by the tip, thus shows no preferred spreading direction. Moreover, the effect of the structural parameters on the wetting behavior is also investigated. It is found that the anisotropy becomes weaker as the height of the shell decreases, which results from the fact that the structured surface becomes close to a planar surface as the height decreases (Supplementary Fig. S3 online).

When the half-cone nanoshell array is modified with $-OH$ by the treatment in O_2 plasma and thus becomes hydrophilic, water propagates in a single preferred direction along the slanting direction and pins in all others, showing the property of uni-directional liquid spreading (Figure 3). As shown in Figure 3A (the nanoshells slant to $-X$), the left contact line advances fast at a speed of 6 mm/s, while the other pins at the surface for the whole process (Supplementary Video 9 online). In contrast, no spreading takes place along the Y direction with a monotonous decrease in the CA (Figure 3B, Supplementary Video 10 online). Figure 3C shows the evolution of the baselines in the X-Z (Figure 3A) and Y-Z (Figure 3B) planes. Only the left baseline advances and all other baselines have no changes, showing the well-defined uni-directional liquid spreading. Besides, the CA in the X-Z plane (Figure 3D) and Y-Z plane (Figure 3E) both decrease as water spreads and become stable when stopping moving. It is needed

to be noted that the preferred direction of the hydrophilic surface is opposite to that of the hydrophobic surface discussed in Figure 1 and 2.

In terms of the reversal in water moving direction based on the changed surface wetting property, PNIPAAm which is a well-known thermo-responsive polymer is grafted on the surface to switch the chemistry of the surfaces and further realize the *in-situ* and immediate control of the liquid flow. This polymer switches from hydrophobic to hydrophilic below its lower critical solution temperature (LCST) of $\sim 32^\circ C$. Figure 4A shows the SEM image of the half-cone nanoshell array modified with PNIPAAm. The polymer is uniformly polymerized on the surface. The schematic in Figure 4B shows the components of the sample. In particular, the layer of Si is deposited to conveniently grow the PNIPAAm. In the beginning the water is injected ($1 \mu L/s$) continuously at the temperature (T) lower than the LCST, the surface is hydrophilic, and the water spreads towards the slanting direction ($-X$), shown in Figure 4C. When T is higher than the LCST, the surface becomes hydrophobic. The water stops spreading and the CA is increasing as the liquid volume increases (Figure 4D). As the water continues to be injected, as shown in Figure 4E, the water moves into the opposite direction, and the left contact line remains pinned at the same position in Figure 4C and D. The whole process can be seen in Supplementary Video 11 online. An inverse process is observed when T changes from high temperature to low temperature, shown in Figure 4(F-H) (Supplementary Video 12 online). The water spreads to $+X$ when T is higher than the LCST in Figure 4F. As the temperature decreases below the LCST, the water pins at the $+X$ side and spreads to $-X$ spontaneously, shown in

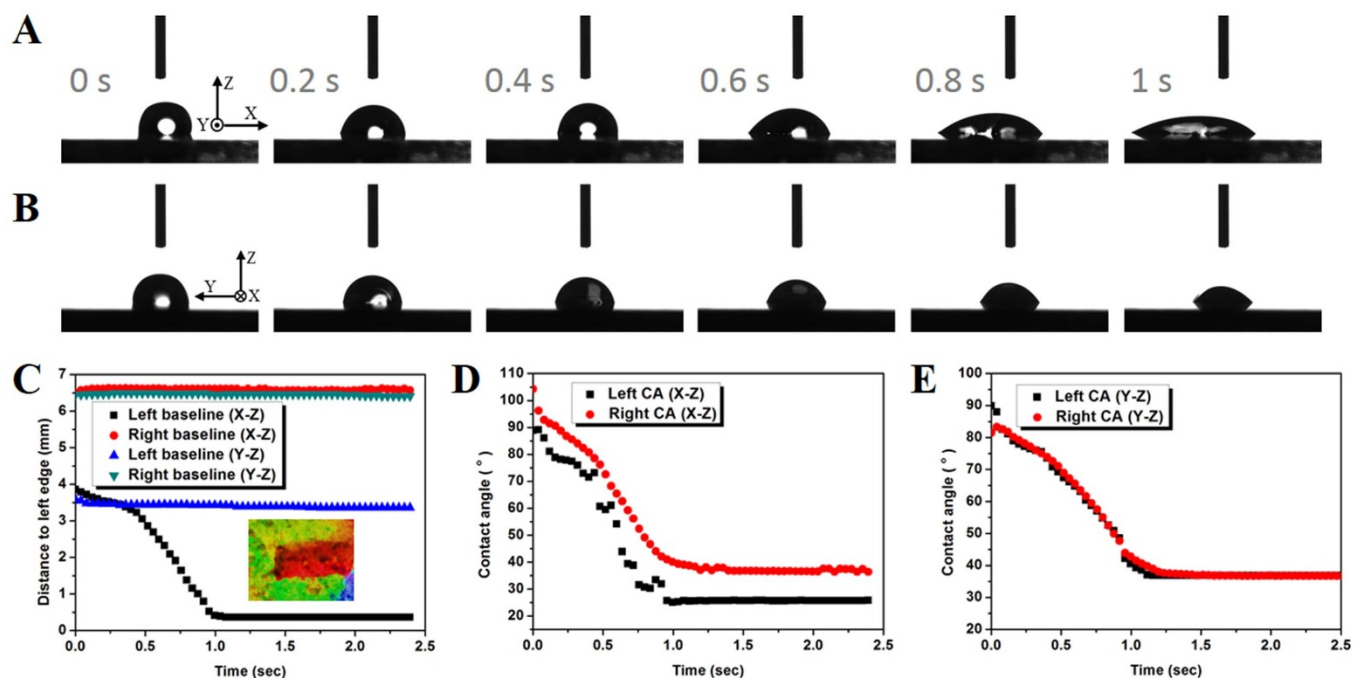


Figure 3 | Uni-directional spreading on the hydrophilic half-cone nanoshell array. *In-situ* photographs of uni-directional wetting in the (A) X-Z plane and (B) Y-Z plane. The nanoshells slant to $-X$. The photographs are taken by every 0.2 s. (C) The evolution of the baselines in the X-Z and Y-Z planes. The inset image shows the optical image of water spreading from the top view. The red part is the water droplet. Evolution of the CA in the (D) X-Z plane and (E) Y-Z plane.

Figure 4G. As the water is injected continuously in Figure 4J, the water still pins at the right side and continues moving towards the $-X$. The two processes can be repeated and cycled as the temperature alternates (Supplementary Video 13 online). It is noticed that the water spreading direction is determined by the wetting property of PNIPAAm which responds to LCST immediately. As soon as the wetting property of PNIPAAm changes from hydrophilicity to hydrophobicity at a certain contact angle, the working mechanism

changes and the water spreading direction switches. The change of contact angle is real-time as the wetting property of PNIPAAm continuously changes, leading to the real-time control of the spreading direction. In other words, the response to a certain contact angle which determines the transition of the two mechanisms is real-time. In this work, we present the concept of real-time responses to a certain wetting case, not to the changing process of temperature. Besides, the operation that the switches of the water spreading dir-

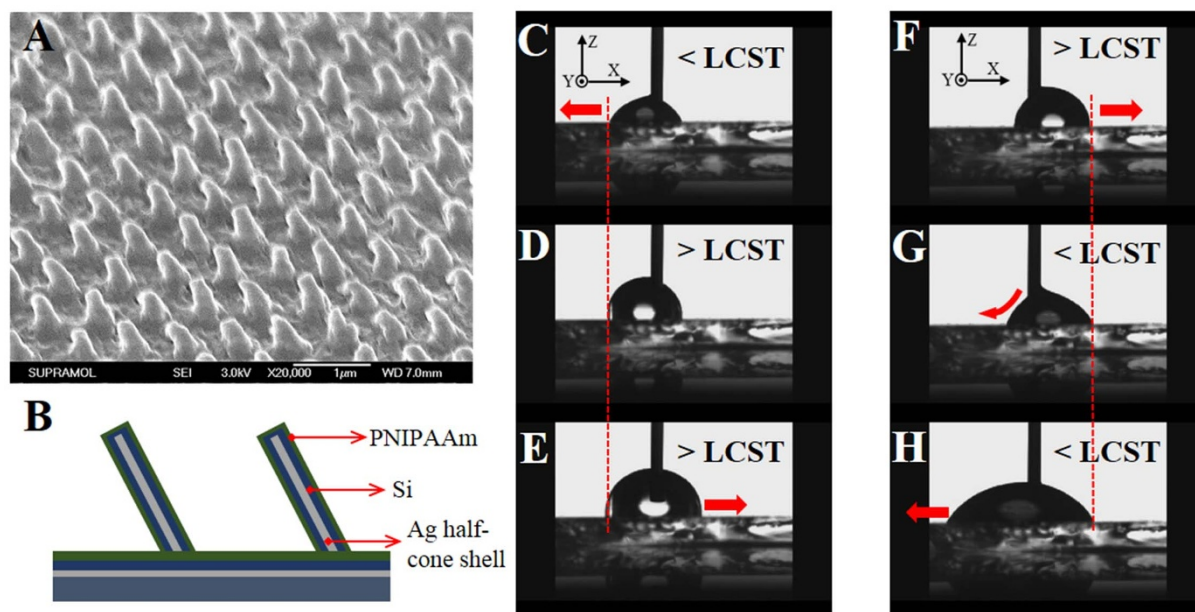


Figure 4 | Control of water spreading direction. (A) SEM image of the half-cone nanoshell arrays modified with PNIPAAm. (B) Schematic diagram showing the components of the sample. Photographs of the water droplet taken at different time as T changes (C–E) from low temperature to high temperature and (F–H) from high temperature to low temperature. The red dotted lines in (C–H) indicate the unchanged pinned positions. The nanoshells slant to $-X$.



ection were demonstrated by the stopping liquid supply in the videos is for more clarity of the whole process. The switches for continuous flow were also easily realized, which can be seen in the second half of Supplementary Video 12 online.

Discussion

The asymmetric wetting property is demonstrated to depend on the asymmetric nanostructure. For the experiments shown in Figure 1 and 2, the Ag-deposited surface is rather rough due to the deposition process. The CA of the planar Ag-deposited surface is 104° because of the rough surface, which lends the sample hydrophobicity (Supplementary Fig. S4 online). Though the fabricated asymmetric nanocones are 3D, they are simplified as slanting rectangles (Figure 5A and B) and triangles (Figure 5C) in two dimensions for easier understanding of the mechanism. For the air (left) side of the half-cone nanoshell, the contact line is discontinuous and the energy barrier is higher than that for movement to the nanoshell side (Figure 5A). Therefore the water droplet prefers to slide along the ridge of the half-cone nanoshell, leading to the advancing force F_{adv} . The interspace of the half-cone nanoshell is then filled with water, which fits to the Wenzel model. There is also strong adhesion force between the surface and water, resulting in the pinning force F_{pin} . When a droplet touches the substrate, the center of gravity is high relative to the following spreading state. This makes F_{adv} larger than F_{pin} , leading to the right shift. As water spreads, the height of the center of gravity decreases, which reduces the potential energy. This would reduce F_{adv} . When the pinning force F_{pin} is equal to the advancing force F_{adv} , the droplet is in an equilibrium state, but still shows the right spreading trend. So the right CA (97°) is larger than the left CA (85°) in the static state, as shown in Figure 1B.

Figure 5B and C show schematic illustrations of the quantitative mechanism involved in the directional liquid flow, which are along the X-Z and Y-Z planes, respectively. As discussed earlier the front of the moving liquid pins at the shell edge, and the pinning is maintained even on increasing the liquid volume until the contact angle of the liquid front reaches its critical contact angle at the edge^{21,33}. If the water overcomes energy barrier at the pinning front, it would spread on the shell surface (solid-vapor interface). According to the geometry in Figure 5B, the critical contact angle θ_c can be written as follows:

$$\theta_{1,c} = \theta + 180^\circ - \beta \quad (1)$$

$$\theta_{2,c} = \theta + \beta \quad (2)$$

where θ is the equilibrium contact angle on a 72° tilting planar surface and β is the included angle between the Ag shell and the planar substrate, which is 72° . As a result, $\theta_{1,c}$ is much larger than $\theta_{2,c}$. Therefore for the X-Z plane, the water front is forced to move into the direction of the lower critical contact angle (the side of the Ag shell) as the liquid volume is increased, leading to the results in Figure 2A. However in Figure 1D, the advancing CA is less than the pinning CA. This results from that the needle at the pinning position would much increase the left CA due to the injection force. For the Y-Z plane (Figure 5C), the nanostructure is symmetric and the critical contact angles are both the same as $\theta_{2,c}$. So there is no directional water spreading along the Y-Z plane, as shown in Figure 2C.

Moreover according to the spreading speed calculated from Figure 2, schematic of the advancing contact line from the top view is presented in Figure 5D. The long axis along the X direction would be three times more than the short axis along the Y direction. This can be seen in the optical images of the directional water drops taken along the X-Z and Y-Z planes. Besides, for the photoresist/Ag nanocone array where Ag is more hydrophobic than the photoresist (Supplementary Fig. S5 online), the water droplet moves towards the photoresist side whose critical contact angle is lower than the Ag side (Supplementary Video 14 online). This also supports the energy argument induced by the asymmetric structure. Overall when the surface of the half-cone nanoshell array is hydrophobic, the water spreads against the nanopillar tilt due to the differences in the energy barrier between the air and Ag shell sides.

When the surface is hydrophilic in Figure 3, water uni-directionally spreads to the slanting direction of the nanoshells (Figure 6A), which is in contrast to the advancing direction on the hydrophobic surface. An entirely different mechanism relative to that of the hydrophobic surface is responsible for the wetting behavior of the hydrophilic surface. According to previous discussions²², a simple two-dimensional model (along the X and Z axes) was developed to explain the behavior of the liquid film in the experiments, shown in Figure 6B. The model assumes that the liquid film propagates only if the contact line is able to reach the next row of pillars. In this case, the local contact angle of the liquid, which is the intrinsic contact angle, θ_{eq} , according to Young's equation, must be equal to or smaller than a critical angle defined as θ_{cr} , shown in Figure 6B. If $\theta_{cr} > \theta_{eq}$, the

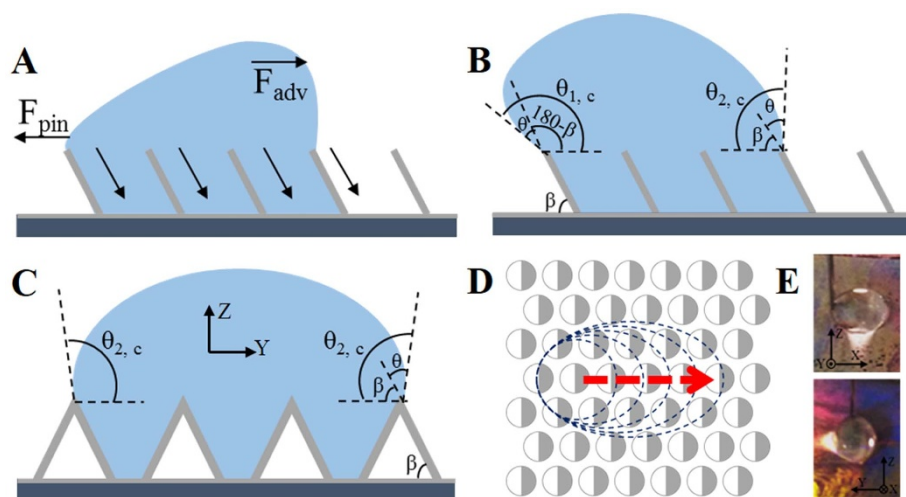


Figure 5 | Mechanism of water spreading on a hydrophobic half-cone nanoshell array. (A–C) Schematic illustrations of the mechanism involved in the directional liquid spreading. The planes in (A, B) are along X-Z; the plane in (C) is along Y-Z. (D) Schematic of the advancing contact line in the X-Y plane. The red arrow indicates the moving direction. (E) Optical images of the directional water drops, which are taken along the X-Z and Y-Z planes, respectively. The nanoshells slant to $-X$.



liquid film propagates within the nanopillars, otherwise, the liquid film pins. In other words, the difference between $\theta_{cr, 1}$ and $\theta_{cr, 2}$ enables uni-directional liquid spreading, only if $\theta_{cr, 2} < \theta_{eq} < \theta_{cr, 1}$.

However, the condition in this work is different from that of the previous work, because the array herein is hexagonally arranged and the lattice orientation may be varied due to the salient features of the CL technique. The relative direction between the slanting Ag shells and the lattice orientation is hardly controllable. Hence there may be more than one nearest shell around, as shown in Figure 6C. Which direction will the water move towards? This problem has not been investigated. We assume that the forces of moving towards the nearest shells are F_n (F_1 , F_2 , and F_3), and the included angles are α_n (α_1 , α_2 and α_3). According to the geometry shown in Figure 6C, α_2 and α_3 are given by:

$$\alpha_2 = \alpha_1 + 60^\circ \quad (3)$$

$$\alpha_3 = 60^\circ - \alpha_1 \quad (4)$$

According to the geometry shown in Figure 6D, ϕ_n which is the slanting angle of the virtual shell projected to the theoretical moving direction is given by:

$$\tan \phi_n = \tan \phi \times \cos \alpha_n \quad (5)$$

where ϕ is the slanting angle of the real shell. The subscript n represents the corresponding moving direction. According to Figure 6E, when a small quantity of water climbs up along the shell, the advancing force dF_n is assumed as:

$$dF_n = \tan \phi_n dG \quad (6)$$

where dG is the gravity force of the small quantity of the rising water. This equation is a simplified one, ignoring other forces. The assumption is also in agreement with the fact that the water is easier to spread as the slanting angle increases²². The three forces F_1 , F_2 , and F_3 can be decomposed into two orthogonal forces, which are along the red arrow (the slanting direction) and the black line in Figure 6C. Combining the above equations, the resultant force dF along the black line in Figure 6C is given by:

$$dF = \sin \alpha_1 dF_1 + \sin \alpha_2 dF_2 - \sin \alpha_3 dF_3 \quad (7)$$

$$= \tan \phi \cos \alpha_1 \sin \alpha_1 dG + \tan \phi \cos (\alpha_1 + 60^\circ) \sin (\alpha_1 + 60^\circ) dG$$

$$- \tan \phi \cos (60^\circ - \alpha_1) \sin (60^\circ - \alpha_1) dG = 0$$

Thus the spreading direction would be always along the slanting direction and independent of the lattice orientation, no matter what the relative direction between the shell and the lattice orientation is. This is also in accord with the experimental result which shows uni-directional spreading in a large area, although where the lattice orientation cannot be uniform (the inset optical image in Figure 3C). Therefore, θ_{cr} can be calculated under the condition that the shell just slants to the near one, not the interspacing between the two near shells. According to the geometry in Figure 6B, $\theta_{cr, 1}$ and $\theta_{cr, 2}$ is given by:

$$\tan \theta_{cr, 1} = \frac{H}{P - R} \quad (8)$$

$$\tan \theta_{cr, 2} = \frac{H}{P + R} \quad (9)$$

$\theta_{cr, 1}$ is calculated as 51° and $\theta_{cr, 2}$ is 33° . The θ_{eq} of the Ag-deposited planar surface with -OH groups is measured as 43° which satisfies the equation $\theta_{cr, 2} < \theta_{eq} < \theta_{cr, 1}$. When the surface is sputtered with Si, the θ_{eq} becomes 27° and the water doesn't show directional propagation. This result also supports the theory. Overall, the experimental data provide excellent agreement with the theory based on an energy argument. In this work, we develop the previous theories based on tetragon-arranged array and apply them to a hexagon-arranged array which is much more complicated. The development of the theory to hexagon-arranged array is significant because of the fact that the hexagon-arranged array is more generally fabricated via unconventional fabrication techniques with the procedure of self-assembly, such as colloidal lithography. So the developed theories in this work would be a foundation for analyzing directional liquid spreading based on slanting structures in hexagonal arrangement.

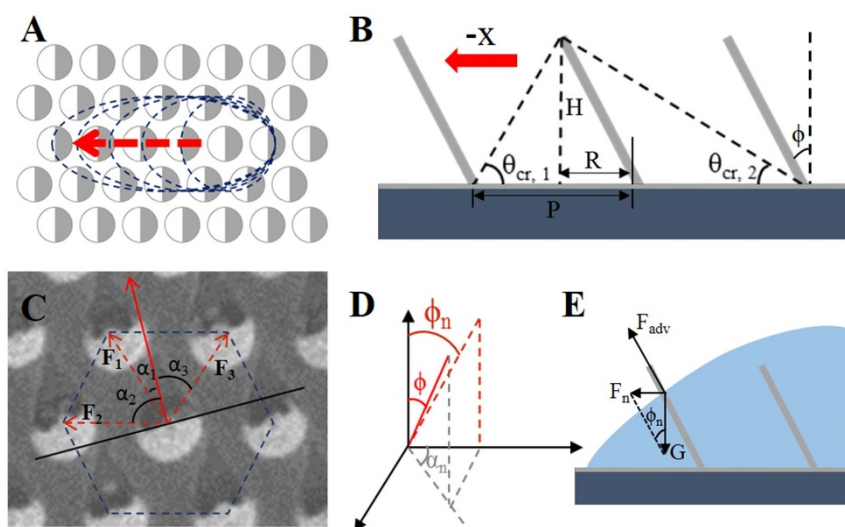


Figure 6 | Mechanism of water spreading on a hydrophilic half-cone nanoshell array. (A) Schematic of the moving contact line from the X-Y plane. The red arrow indicates the spreading direction. (B) Schematic diagram explaining the geometries for the proposed model to determine the critical angle, θ_{cr} , in the -X (left) and +X (right) directions. The blue arrow indicates the moving direction. The period $P=700$ nm, the radius $R=200$ nm and the height $H=600$ nm. (C) Schematic diagram on the SEM image showing the real slanting direction (red solid arrow), the possible moving directions (red dotted arrows) and the included angles. The SEM image is taken from a top view. (D) Schematic diagram showing the slanting angles of the shell projected to the possible moving directions. (E) Schematic diagram showing the relationship between the moving force F and the gravity G .



According to the above discussions for the hydrophobic and hydrophilic surface, the mechanism of controlling water spreading direction on the PNIPAAm coated sample (Figure 4) can be well explained. When T is below the LCST, the θ_{eq} of the PNIPAAm on the Ag-deposited planar surface is measured as 40° (Supplementary Fig. S6 online) which satisfies the equation $\theta_{cr, 2} < \theta_{eq} < \theta_{cr, 1}$. Therefore, the mechanism in Figure 6 works and the water spreads to the slanting direction. When T is higher than the LCST, θ_{eq} becomes 70° (Supplementary Fig. S6 online) and PNIPAAm is hydrophobic. For the hydrophobic surface of the half-cone nanoshell array, the mechanism concluded from Figure 5 that the water spreads against the nanopillar tilt works. So the water spreads to the reverse side. Overall, the water spreading direction can be real-time controlled by tuning the temperature based on the two different mechanisms. Besides, other fluids with various surface tensions, such as ethanol and toluene, also were tested on the nanostructure. The θ_{eq} is so small that it is lower than $\theta_{cr, 2}$, so the liquids do not show directional propagation. This also supports the theory concluded from Figure 6. Furthermore, the results also mean that PNIPAAm cannot make the θ_{eq} of ethanol and toluene satisfy the equation $\theta_{cr, 2} < \theta_{eq} < \theta_{cr, 1}$. If desired material which can increase the θ_{eq} to satisfy the equation is grafted on the surface, this system works as well to realize the directional propagation of other various liquids. So directional spreading for various liquids would be realized based on the structure in this work with proper materials. This indicates a promising prospect for the extension of the half-cone nanoshell Array.

In summary, real-time (*in-situ* and immediate) control of uni-directional liquid spreading is realized based on tilted half-cone nanoshell arrays. The nanostructures are fabricated simply and efficiently via colloidal lithography which is capable of patterning large areas in parallel at low cost. The wetting property of the surface determines the direction of liquid movement, which can be well explained by two entirely different mechanisms. In particular, the finding that the spreading direction on a hexagonal cone array does not depend on the lattice orientation and only on the slanting direction is explained theoretically. To expand on the above findings, PNIPAAm is grafted on the structured surface to control the liquid flow in real time. The combination with the functional polymer results in deeper exploitation of the nanostructures. The inclined half-cone nanoshell arrays are very promising systems because of their high precision and ease of manufacturing to achieve uni-directional liquid spreading. Moreover, other materials or polymer with the ability of switching between hydrophobicity and hydrophilicity, instead of the PNIPAAm used in this work, are believed to realize the real-time control of the uni-directional liquid spreading on the half-cone nanoshell arrays as well. This means the preferred direction on the array can be well controlled by the certain factor corresponding to the using responsive materials, like light, pH, *et al.* The findings gained from this work offer new opportunities for smart microfluidics, water harvesting and other wetting conditions on demand.

Methods

Fabrication of half-cone nanoshell arrays. Photoresist was spin-coated onto the glass substrate and cured at 88°C for 2 h. Next the PS sphere (700 nm) monolayers were prepared onto the as-prepared substrate by the interface method³⁴. Oxygen reactive ion etching (RIE), performed on a Plasmalab Oxford 80 Plus system (ICP 65) system (Oxford Instrument Co., UK), was applied for 240, 270 and 300 s, eliminating the PS spheres and generating cones with heights of 600, 500 and 400 nm. The RIE procedure was operated at a pressure of 10 mTorr, a flow rate of 50 sccm, a radio-frequency (RF) power of 100 W and an inductively coupled plasma (ICP) power of 200 W. After that the samples were mounted in a thermal evaporator to deposit 100-nm Ag with an angle of 40° . Finally the photoresist was washed away by ethanol. After these procedures, the half-cone nanoshell array was formed.

Modification of the Surface. Trichloro(1H, 1H, 2H, 2H-perfluorooctyl)silane (PFS) is grafted onto the surface through chemical vapor deposition. Firstly, a layer of silicon was deposited on the surface by a sputtering process. After that, the wafers were placed in an oxygen plasma to make the surface full of -OH groups. These as-prepared samples were placed in a sealed vessel, on the bottom of which were a few drops of PFS. There was no direct contact between the drops and wafers. The vessel

was put in an oven at 60°C for 5 h to enable the PFS vapor to react with the -OH groups.

Synthesis of pnipaaam thin films on half-cone nanoshell arrays. PINIPAAm was grown on the sample by surface-initiated atom-transfer radical polymerization (SI-ATRP)³⁵. Firstly, a layer of silicon was deposited on the surface by a sputtering process. After that, the wafers were placed in an oxygen plasma to achieve a high surface density of -OH groups. The -NH₂ groups were grafted onto the surface by a gas-phase growth method. In brief, these as-prepared samples were placed in a sealed vessel, on the bottom of which were a few drops of aminopropyltrimethoxysilane (ATMS). There was no direct contact between the drops and the wafers. The vessel was put in an oven at 60°C for 1 h to enable the ATMS vapor to react with the -OH groups. These wafers with -NH₂ were immersed in a solution of 10 mL anhydrous dichloromethane with 140 μL triethylamine. The mixture is left for 10 min at 0°C . The ATRP initiator, 100 μL 2-bromoisobutyl bromide, was added dropwise into the solution containing the wafers with -NH₂ at 0°C , and the mixture is left for 1 h at this temperature, then at room temperature for 15 ~ 18 h. The wafers were cleaned by anhydrous dichloromethane three times and absolute ethanol three times, and dried by N₂ flow.

For polymerization of poly(N-isopropyl-acrylamide) (PNIPAAm) from the ATRP initiators, 0.3 g of NIPAAm (2.65 mmol) and 140 μL 1,1,4,7,7-pentamethyldiethylenetriamine (PMDETA) (0.67 mmol) were added to 5 mL of an aqueous solution (CH₃OH/H₂O, 1 : 1 v/v), and the mixtures were shaken in an ultrasonic bath until a homogeneous transparent solution formed. The mixtures were degassed by 30 min ultrapure nitrogen flow, 22 mg CuCl (0.22 mmol) was added into the solution, and the solution was shaken in an ultrasonic bath and changed into green, at last the wafers with initiators were immersed into the solution for 1 h under nitrogen flow at room temperature. After polymerization, the samples were cleaned by absolute ethanol and deionized water for several times. Under these conditions, the film thickness was about 60 nm.

Characterization. Scanning electron microscopy (SEM) images were taken with a JEOL JSM 6700F field emission scanning electron microscope with a primary electron energy of 3 kV, and the samples were sputtered with a layer of Pt (about 2 nm thickness) prior to imaging to improve the conductivity. Water CAs were measured with an OCA20 machine (DataPhysics, Germany) at saturated humidity. The temperature was controlled by a superthermostat (Julabo F25, Germany).

- Zhang, F. X. & Low, H. Y. Anisotropic wettability on imprinted hierarchical structures. *Langmuir* **23**, 7793–7798 (2007).
- Semprebon, C. *et al.* Anisotropy of water droplets on single rectangular posts. *Langmuir* **25**, 5619–5625 (2009).
- Zhao, Y., Lu, Q. H., Li, M. & Li, X. Anisotropic wetting characteristics on submicrometer-scale periodic grooved surface. *Langmuir* **23**, 6212–6217 (2007).
- Higgins, A. M. & Jones, R. A. L. Anisotropic spinodal dewetting as a route to self-assembly of patterned surfaces. *Nature* **404**, 476–478 (2000).
- Kusumaatmaja, H., Vrancken, R. J., Bastiaansen, C. W. M. & Yeomans, J. M. Anisotropic drop morphologies on corrugated surfaces. *Langmuir* **24**, 7299–7308 (2008).
- Liu, H., Zhai, J. & Jiang, L. Wetting and anti-wetting on aligned carbon nanotube films. *Soft Matter* **2**, 811–821 (2006).
- Quééré, D. Non-sticking drops. *Rep. Prog. Phys.* **68**, 2495–2532 (2005).
- Öner, D. & McCarthy, T. J. Ultrahydrophobic surfaces. Effects of topography length scales on wettability. *Langmuir* **16**, 7777–7782 (2000).
- Cai, Y. *et al.* Filefish-inspired surface design for anisotropic underwater oleophobicity. *Adv. Funct. Mater.* **24**, 809–816 (2014).
- Seemann, R., Brinkmann, M., Kramer, E. J., Lange, F. F. & Lipowsky, R. Wetting morphologies at microstructured surfaces. *Proc. Natl Acad. Sci.* **102**, 1848–1852 (2005).
- Maritines, E. *et al.* Superhydrophobicity and superhydrophilicity of regular nanopatterns. *Nano Lett.* **5**, 2097–2103 (2005).
- Dupuis, A., Léopoldès, J., Bucknall, D. G. & Yeomans, J. M. Control of drop positioning using chemical patterning. *Appl. Phys. Lett.* **87**, 024103 (2005).
- Gleiche, M., Chi, L. F. & Fuchs, H. Nanoscopic channel lattices with controlled anisotropic wetting. *Nature* **403**, 173–175 (2000).
- Zhang, T. *et al.* Bio-inspired anisotropic micro/nano-surface from a natural stamp: grasshopper wings. *Soft Matter* **7**, 7973–7975 (2011).
- Chen, Y., He, B., Lee, J. & Patankar, N. A. Anisotropy in the wetting of rough surfaces. *J. Colloid Interface Sci.* **281**, 458–464 (2005).
- Drelich, J., Wilbur, J. L., Miller, J. D. & Whitesides, G. M. Contact angles for liquid drops at a model heterogeneous surface consisting of alternating and parallel hydrophobic/hydrophilic strips. *Langmuir* **12**, 1913–1922 (1996).
- Gau, H., Herminghaus, S., Lenz, P. & Lipowsky, R. Liquid morphologies on structured surfaces: from microchannels to microchips. *Science* **283**, 46–49 (1999).
- Chung, J. Y., Youngblood, J. P. & Stafford, C. M. Anisotropic wetting on tunable micro-wrinkled surfaces. *Soft Matter* **3**, 1163–1169 (2007).
- Xia, D. Y. & Brueck, S. R. J. Strongly anisotropic wetting on one-dimensional nanopatterned surfaces. *Nano Lett.* **9**, 2819–2823 (2008).



20. Gao, X. F., Yao, X. & Jiang, L. Effects of rugged nanoprotusions on the surface hydrophobicity and water adhesion of anisotropic micropatterns. *Langmuir* **23**, 4886–4891 (2007).
21. Kim, S. M. *et al.* Thermo-responsive switching of liquid flow direction on a two-face prism array. *Soft Matter* **9**, 4145–4149 (2013).
22. Chu, K. H., Xiao, R. & Wang, E. N. Uni-directional liquid spreading on asymmetric nanostructured surfaces. *Nat. Mater.* **9**, 413–417 (2010).
23. Kim, T. I. & Suh, K. Y. Unidirectional wetting and spreading on stooped polymer nanohairs. *Soft Matter* **5**, 4131–4135 (2009).
24. Kwak, M. K., Jeong, H. E., Kim, T., Yoon, H. & Suh, K. Y. Bio-inspired slanted polymer nanohairs for anisotropic wetting and directional dry adhesion. *Soft Matter* **6**, 1849–1857 (2010).
25. Malvadkar, N. A., Hancock, M. J., Sekeroglu, K., Dressick, W. J. & Demirel, M. C. An engineered anisotropic nanofilm with unidirectional wetting properties. *Nat. Mater.* **9**, 1023–1028 (2010).
26. Kubus, L., Erdogan, H., Piskin, E. & Demirel, G. Controlling uni-directional wetting via surface chemistry and morphology. *Soft Matter* **8**, 11704–11707 (2012).
27. Yang, X. M. *et al.* Asymmetric liquid wetting and spreading on surfaces with slanted micro-pillar arrays. *Soft Matter* **9**, 11113–11119 (2013).
28. Zhang, G., Wang, D. & Möhwald, H. Fabrication of multiplex quasi-three-dimensional grids of one-dimensional nanostructures via stepwise colloidal lithography. *Nano Lett.* **7**, 3410–3413 (2007).
29. Zhang, G. & Wang, D. Colloidal lithography—the art of nanochemical patterning. *Chem.-Asian J.* **4**, 236–245 (2009).
30. Ai, B., Yu, Y., Möhwald, H., Zhang, G. & Yang, B. Plasmonic films based on colloidal lithography. *Adv. Colloid Interface Sci.* **206**, 5–16 (2014).
31. Wenzel, R. N. Resistance of solid surfaces to wetting by water. *Ind. Eng. Chem.* **28**, 988–994 (1936).
32. Cassie, A. B. D. & Baxter, S. Wettability of porous surfaces. *Trans. Faraday Soc.* **40**, 546–551 (1944).
33. Young, T. An essay on the cohesion of fluids. *Philos. Trans. R. Soc. Lond.* **95**, 65–87 (1805).
34. Rybczynski, J., Ebels, U. & Giersig, M. Large-scale, 2D arrays of magnetic nanoparticles. *Colloids Surf. A* **219**, 1–6 (2003).
35. Barbey, R. *et al.* Polymer brushes via surface-initiated controlled radical polymerization: synthesis, characterization, properties, and applications. *Chem. Rev.* **109**, 5437–5527 (2009).

Acknowledgments

This work was supported by the National Natural Science Foundation of China (51073070, 51173068, 51373066) and “111” project (B06009).

Author contributions

B.A. and G.Z. designed the experiments. B.A. prepared the samples and performed the characterizations. L.W. assisted in fabricating the structure. H.M., Y.Y. and Z.Z. assisted in data analysis. Z.Z. assisted in synthesis of PNIPAAm thin films. The manuscript was prepared by B.A. and G.Z. with assistance from H.M., Y.Y. and Q.L. All authors reviewed the manuscript.

Additional information

Supplementary information accompanies this paper at <http://www.nature.com/scientificreports>

Competing financial interests: The authors declare no competing financial interests.

How to cite this article: Ai, B. *et al.* Real-Time Control of Uni-Directional Liquid Spreading on a Half-Cone Nanoshell Array. *Sci. Rep.* **4**, 6751; DOI:10.1038/srep06751 (2014).



This work is licensed under a Creative Commons Attribution-NonCommercial-NoDerivs 4.0 International License. The images or other third party material in this article are included in the article's Creative Commons license, unless indicated otherwise in the credit line; if the material is not included under the Creative Commons license, users will need to obtain permission from the license holder in order to reproduce the material. To view a copy of this license, visit <http://creativecommons.org/licenses/by-nc-nd/4.0/>